PROGRESS IN COLOR, COLORANTS AND COATINGS

available online @ www.pccc.icrc.ac.ir

Progress in Color Colorants Coating 19 (2026), 113-133

Ministry of Science, Research and Technology
Institute for Color Science & Technology

Coating $Ti_{13}Nb_{13}Zr$ Alloy with Hydroxyapatite Using Pyrolysis Spray Improves Corrosion and Osseointegration Characteristics for Biomedical Applications (In-vitro study)

G. Hamed Farhan[1], J. Abduljabar Hassan[1], A. H. Al-helli[*2]

[1.] Department of Biomedical Engineering, College of Engineering, Al-nahrain University, P.O. Box: 62021, Baghdad, Iraq.

[2.] Department of Unmanned Aerial Vehicle (UAV) Engineering, College of Engineering Al-nahrain University, P.O. Box: 62021, Baghdad, Iraq.

ARTICLE INFO

Article history:
Received: 19 Mar 2025
Final Revised: 09 Aug 2025
Accepted: 12 Aug 2025
Available online: 01 Nov 2025

Keywords:
Titanium alloys
Osseointegation
XRD
FESEM
EDX

ABSTRACT

Titanium and its alloys are widely used in biomedical applications. There are two essential uses in the biomedical field: dental and orthopedic. $Ti_{13}Nb_{13}Zr$ has been predominantly used in orthopedic surgery over the last decade. In this research, $Ti_{13}Nb_{13}Zr$ was coated with hydroxyapatite (HAP) to enhance osseointegration and improve corrosion characteristics. The pyrolysis spray technique was used to apply layers of HAP (2, 3, 4 and 5) on the $Ti_{13}Nb_{13}Zr$ alloy, with a 2-minute interval between each layer to allow for drying. The coating was characterized using XRD, FESEM, and EDX, and its electrochemical corrosion properties were also investigated. The coated samples were immersed in simulated body fluid (SBF) for one month and then tested using the same methods to evaluate the improvement in corrosion and osseointegration characteristics. The results show that coating before immersing in SBF solution was uniform, and the corrosion rate improved, reaching 5.779×10^{-5} mmpy compared with 1.741×10^{-3} mmpy for the uncoated sample, while the protection efficiency reached 96.68 %. After immersing in the SBF solution, the XRD, FESEM, and EDX test results confirm the formation of a new hydroxyapatite layer, and the corrosion rate and protection efficiency reached 3.498×10^{-5} mmpy and 98.27 % respectively. Prog Color Colorants Coat. 19 (2026), 113-133© Institute for Color Science and Technology.

1. Introduction

Titanium and titanium alloys are widely used in biomedical, orthopedic, and dental applications [1]. The use of titanium and its alloys in the orthopedic medical field has been growing significantly due to their mechanical and physical properties, such as good fatigue strength, relatively low modulus, high corrosion resistance, and good biocompatibility [2-4]. To increase corrosion resistance and osseointegration with bones, researchers have conducted studies to improve these two characteristics by coating with bioactive ceramics like hydroxyapatite [5-7]. Hydroxyapatite (HAP) is the main component of the skeletal system and bone structures shown in Figure 1, comprising about 50 % of the weight of bone [8-10]. Coating with hydroxyapatite can first activate the spread of osteoblasts and promote the growth and differentiation of mesenchymal stem cells (MSCs) by increasing the concentration of local Ca^{2+} ions. Second, the structure of HAP is very similar to that of hydroxyapatite in bones, which facilitates bone

*Corresponding author: * ali.h.mohammed@nahrainuniv.edu.iq
https://doi.org/10.30509/pccc.2025.167501.1376

growth [11, 12]. However, surface treatments have been extensively developed to address their low osteoconductivity and enhance their biological properties. The application of hydroxyapatite (HA) coating to titanium alloys represents an effective surface modification technique. The implementation of implants remains one of the most developed and efficient methods to maximize surface enhancements while improving biological properties. The mechanical properties of Ti with the bioactivity of HA [13]. The intended operational duration for implants within human bodies extends between fifteen and twenty years. Implants installed in human tissue face two main challenges from body fluids. The corrosive nature of blood and water, along with sodium, chlorine, proteins, plasma, and amino acids, weakens both implant mechanics and biocompatibility. To prevent implant failure from toxic ions within the body, corrosive resistance should be high in an implant system [14, 15]. Bone regeneration shows its maximum effectiveness with synthetic HA because it contains stoichiometric calcium and phosphorus ratios at 1.67 [16]. Natural HA exists in non-stoichiometric form because it contains various trace elements such as Ba, Si, F, Zn, Mg, K, Na, and CO_3, similar in chemical composition to human bone [16, 17]. Scientists show great interest in Hydroxyapatite ($Ca_{10}(PO_4)_6(OH)_2$) for medical applications because of its superior bioactivity and match with human tissue. Hydroxyapatite has become a highly interesting material for both artificial implants and human tissue restorations because it creates a suitable environment for bone growth near the implant [18]. The synthesis of HaP coatings requires different production methods, including micro-arc oxidation [19], plasma spray [20], physical vapor deposition (PVD), sol-gel, and others.

The spray pyrolysis technique offers various advantages that include uniform coating thickness, high production rate, cost-effectiveness, and the capability to coat intricate shapes and forms. The production of crystalline coatings through this technique becomes possible without requiring any post-heating process [21]. There were many techniques for coating biomedical ceramics on metals and their alloys. The most common and widely used techniques were dip coating, electrophoretic deposition, thermal spray, cold spray, and pyrolysis spray [22-27]. Each technique has its advantages and disadvantages. The pyrolysis spray technique has spread remarkably in the last decade. In our research, we chose pyrolysis spray to coat HAP on

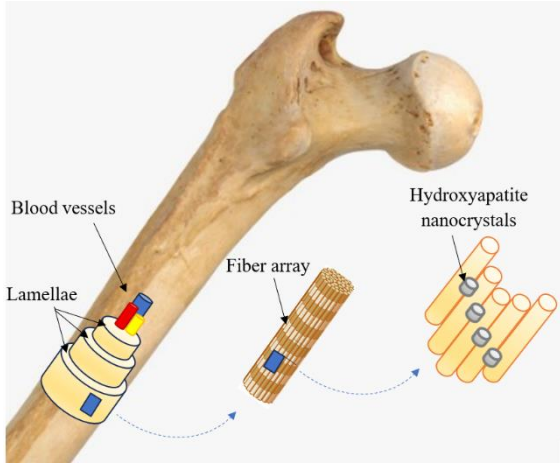

Figure 1: Hydroxyapatite in bone structure.

the $Ti_{13}Nb_{13}Zr$ alloy because it has many advantages, such as uniform coating, easy control during coating, good adhesion, low cost, and very easy use, which does not require specialized skills [28]. The other techniques, such as dip coating, electrophoretic deposition, and cold spray, have the disadvantage of low adhesion for the coated layer.

Additionally, thermal spray provides good adhesion, but the elevated temperatures used reach up to 2500 °C. The $Ti_{13}Nb_{13}Zr$ alloy samples were coated with different numbers of layers (2, 3, 4, and 5). The coated samples were tested using XRD, FESEM, and EDX, and the electrochemical corrosion was also evaluated. The samples were immersed in simulated body fluid (SBF) for one month and then tested with the same methods to evaluate the results. The pyrolysis spray technique coatings on $Ti_{13}Nb_{13}Zr$ alloy demonstrated enhanced corrosion resistance, making them suitable for biomedical applications. The addition of HAp improved corrosion resistance, reducing the corrosion rate significantly compared to uncoated substrates.

2. Experimental

2.1. Materials

The $Ti_{13}Nb_{13}Zr$ alloy rod with a diameter of 20 mm (Baoji, China), as shown in Table 1, was cut into 2 mm-thick disk samples using a wire cutter machine, based on the chemical composition provided by the manufacturing company certificate. The $Ti_{13}Nb_{13}Zr$ alloy was ground using SiC grinding paper with grits ranging from 180 to 500. The samples were then cleaned twice with

96 % ethanol (Sigma Aldrich, USA) and once with distilled water using an ultrasonic cleaner bath (1800 QT, China).

2.2. Methods

The preparation of the coating solution was achieved by dissolving 3 g of polyvinylpyrrolidone (PVP K30, CDH, India) in 10 mL of water, mixing thoroughly until completely dissolved using a magnetic stirrer (VS-130SH, Korea). The PVP provides high adhesion to the coating layer and helps anchor it. Poly-vinylpyrrolidone (PVP) appears to be a suitable material for this purpose. High water-binding properties and high biocompatibility characterize PVP [30, 31]. The volume was then increased to 100 mL by adding 90 mL of absolute ethanol (99 %, Sigma Aldrich, USA) and mixing well. Next, 10 g of hydroxyapatite (<40 nm, Sky Spring Nanomaterials, USA) was added to the mixture and vigorously mixed using the magnetic stirrer. The coating process involved heating the $Ti1_3Nb1_3ZR$ alloy disc to 80 °C for 2 minutes, followed by applying the coating using a spray gun connected to a 5 bar air compressor after filling the gun cup with the coating suspension, as shown in Figure 2. The $Ti_{13}Nb_{13}Zr$ alloy disc was allowed to dry for 2 min after coating each layer. The coating was repeated to achieve 2, 3, 4, and 5 layers. The samples were then tested using XRD, FESEM, and EDX.

Additionally, the contact angle and adhesion tests were conducted. The corrosion test was performed using a potentiostat (CHI 604E, China) to measure the open circuit potential (OCP), polarization curve (Tafel), and electrochemical impedance spectroscopy (EIS) using simulated body fluid (SBF) solution with the chemical composition listed in Table 2 as a corrosion medium. Uncoated and optimally coated samples were immersed in the SBF solution for one month to evaluate osseointegration and biocompatibility. It has been established that the formation of a bone-like HA layer on the surface of an artificial implant is one of the major requirements for the implant to bond well to living bone and tissue [32]. The immersed samples were tested by XRD, FESEM, and EDX, and the corrosion test was conducted by measuring the open circuit potential (OCP), polarization curve (Tafel), and electrochemical impedance spectroscopy (EIS) using simulated body fluid (SBF).

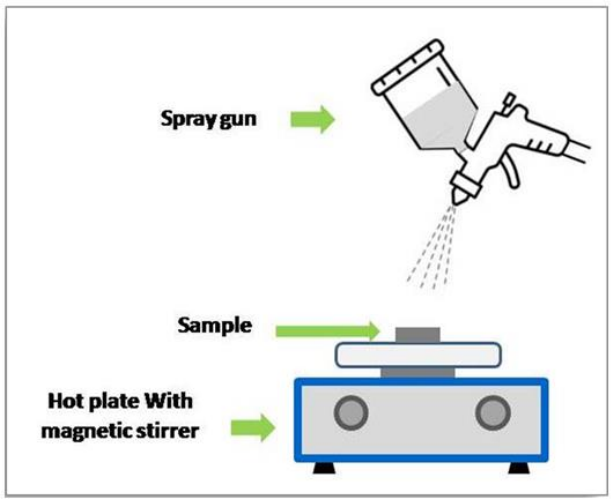

Figure 2: Pyrolysis spray coating system.

Table 1: Chemical composition of $Ti_{13}Nb_{13}Zr$ alloy.

Chemical composition [wt. %]								
Component	Nb	Zr	Fe	C	H	O	S	Ti
As recieed	13.18	13.49	0.085	0.035	0.004	0.078	<0.001	Balanced
standard	12.5 -14	12.5 -14	0.25	0.08	0.12	0.15	0.005	Balanced

Table 2: Chemical composition of simulated body fluid (SBF) solution [33].

ITEM	NaCl	$NaHCO_3$	KCl	K_2HPO_4	$MgCl_2.6H_2O$	$CaCl_2$	Na_2SO_4
Concentration (g/L)	8.035	0.355	0.225	0.231	0.311	0.292	0.072

3. Results and Discussion

3.1. XRD Test

The XRD pattern of the uncoated sample is shown in Figure 3, with the Miller indices labeled for titanium at all peak positions. The XRD pattern for the 2-layer coated sample in Figure 4 shows the peaks of hydroxyapatite and titanium with the Miller indices labeled. The reduction in titanium peaks was due to hydroxyapatite covering the sample surface after coating. titanium according to Miller indices, which represents the sample without coating, while Figure 4 shows a mixture of peaks for titanium and hydroxypeptide according to Miller indices. The appearance of mixed peaks is due to the light thickness of the coating; as we observe when increasing the coating layers, the titanium peaks decrease while the hydroxypeptide peaks increase, as shown in the subsequent figures.

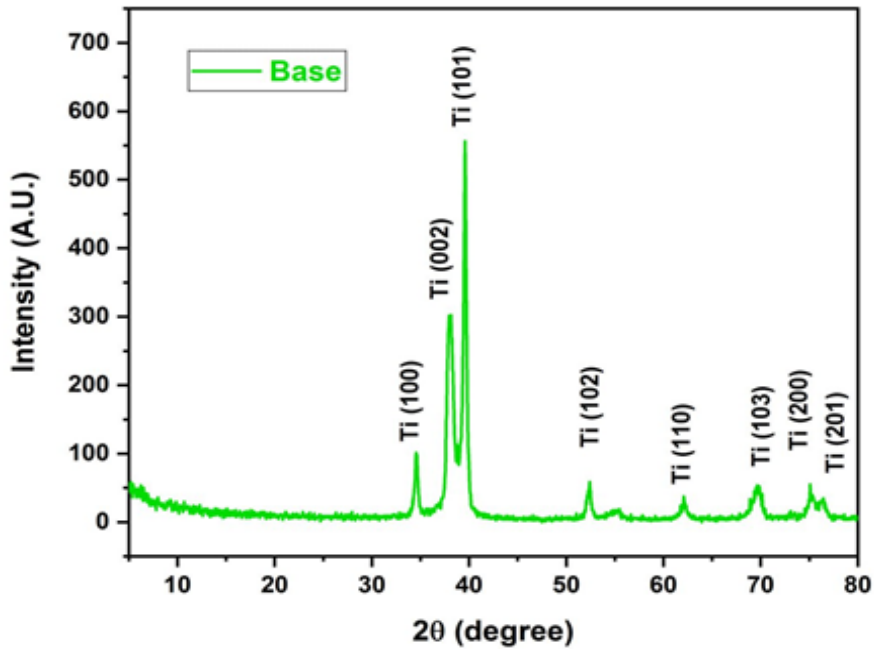

Figure 3: XRD pattern of uncoated $Ti_{13}Nb_{13}Zr$ alloy sample peaks labeled with Miller indices.

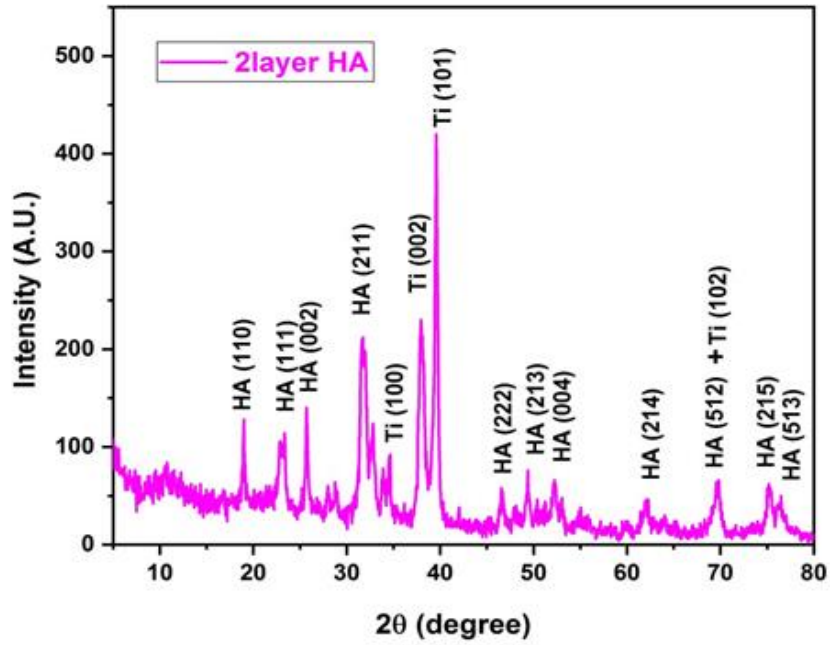

Figure 4: The XRD pattern for the 2-layer coated sample.

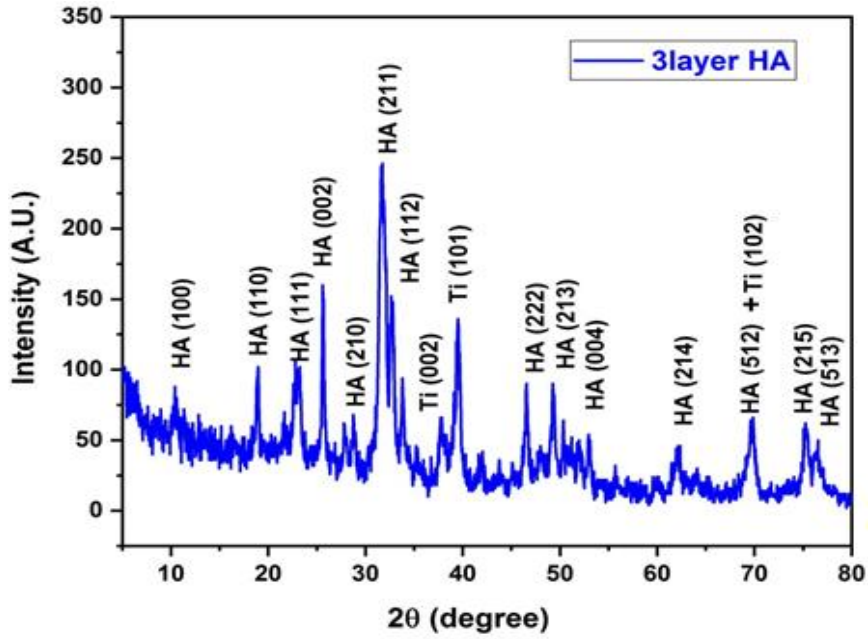

Figure 5: The XRD pattern for the 3-layer coated sample.

The difference between Figures 3 and 4 is that the former contains all the peaks for Figure 5 shows the XRD pattern for the three-layer coated sample. We observe a clear appearance of hydroxyapatite peaks and $Ti_{13}Nb_{13}Zr$ alloy peaks for titanium, with the Miller indices labeled. There is a reduction in the intensity of the titanium peaks compared to the two-layer coated sample XRD pattern, indicating a greater surface coverage by the hydroxyapatite-coated layers.

Figure 6 shows the XRD pattern for the four-layer coated sample. We observe a clear appearance of hydroxyapatite peaks with the Miller indices labeled, as well as the peaks for the $Ti_{13}Nb_{13}Zr$ alloy with the Miller indices labeled for titanium. Additionally, we see a significant reduction in the titanium peaks, which have become only two peaks, indicating greater coverage due to the hydroxyapatite coating.

The XRD pattern for the five-layer coated sample in Figure 7 shows a good appearance of hydroxyapatite peaks and a single peak of titanium. The peaks of hydroxyapatite perfectly match JCPDS File Card No. 00-009-0432 for hydroxyapatite. The significant reduction in titanium peaks is attributed to hydroxy-apatite's excellent coverage of the sample surface after coating.

The comparison of the XRD patterns in Figure 8 for all samples shows an increase in hydroxyapatite intensity compared with a reduction in titanium intensity as the number of layers increases. X-ray diffractometry analysis of HAp coated on a $Ti_{13}Nb_{13}Zr$ substrate was conducted. The XRD pattern of the samples indicates that the coating consists of HAp in multiple layers (2, 3, 4, and 5), which is necessary to improve the material's biocompatibility and osseointegration. The phase of Ti exhibits peak formation at 40º, which decreases with an increasing number of coating layers. The phase of HAp shows peak formation at 31.9º, indicating the presence of the HAp phase. An increase in the peak intensity of HAp was observed with an increasing number of HAp layers on the Ti alloy.

3.2. FESEM test

The FESEM images in Figure 9a-j with two magnifications show a thick coating for all samples. The two-layer sample exhibits a crack in the coating layer, while the three, four, and five-layer samples show a very porous coating layer. This occurs because the two-layer coating has a smaller thickness than the other samples, which is affected by heating, whereas the other samples have greater thickness, which prevents cracks. Additionally, we observe that the measured particle size for the coated samples increased with the increasing number of layers, as shown in Table 3, indicating an increase in agglomeration with the increasing number of coated layers. The FESEM images of HaP coatings are presented after the three

layers. The experimental results show that the sprayed coatings possessed a homogeneous surface without any cracks or holes. Moreover, the HaP particles were evenly distributed throughout the film. It was also noted that the shape and uniformity of the grains were affected by the concentration of doping in the HaP material. At a five-layer doping concentration, the grains were more uniform.

Table 3: Measured particle size from FESEM test.

ITEM	Particle size range (nm)
1- 2 layers	23.92 - 29.24
2- 3 layers	25.00 – 36.75
3- 4 layers	33.82 – 37.07
4- 5 layers	30.40 – 50.06

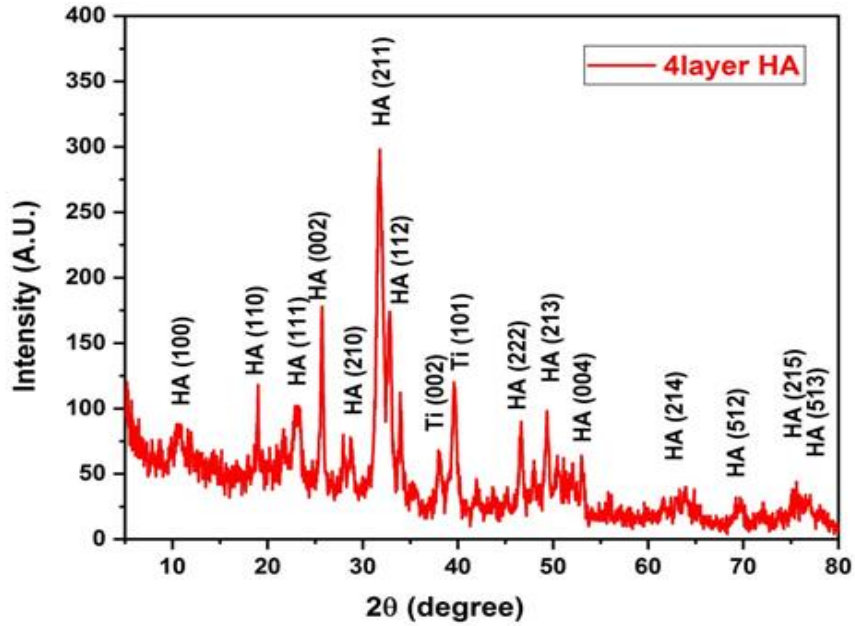

Figure 6: The XRD pattern for the 4-layer coated sample.

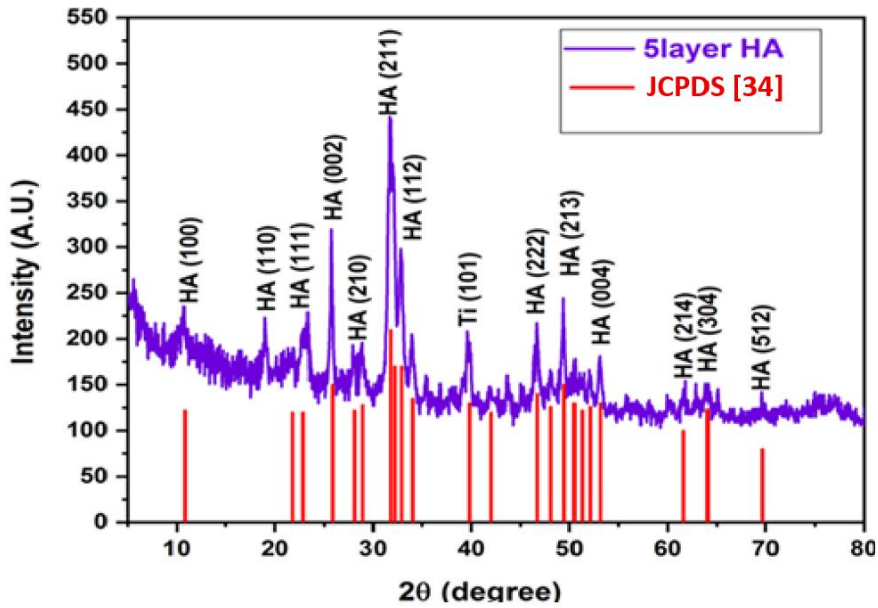

Figure 7: XRD patterns of the five-layer coated sample and JCPDS No. 00-009-0432.

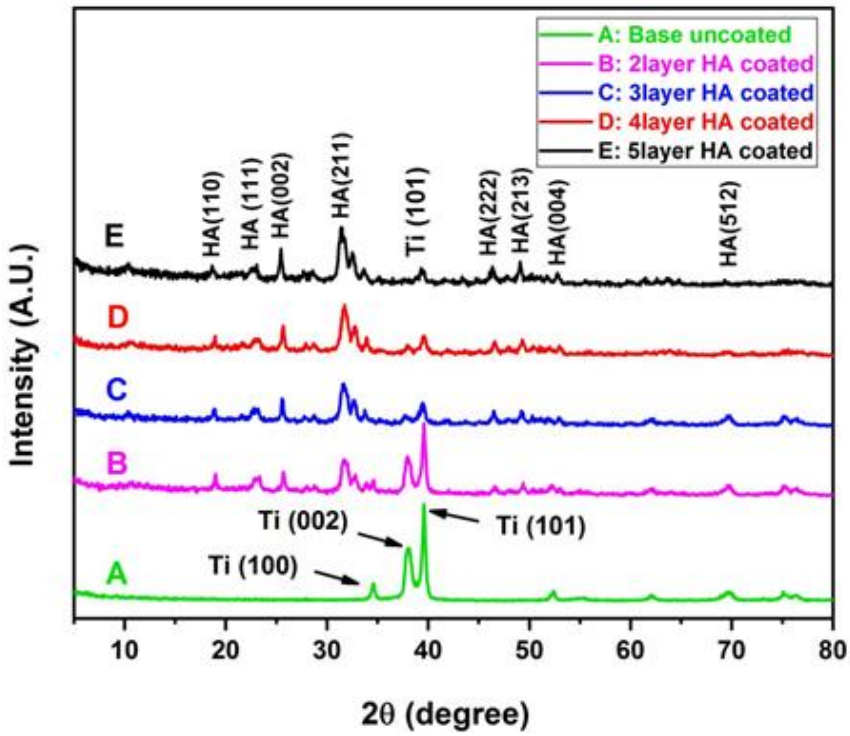

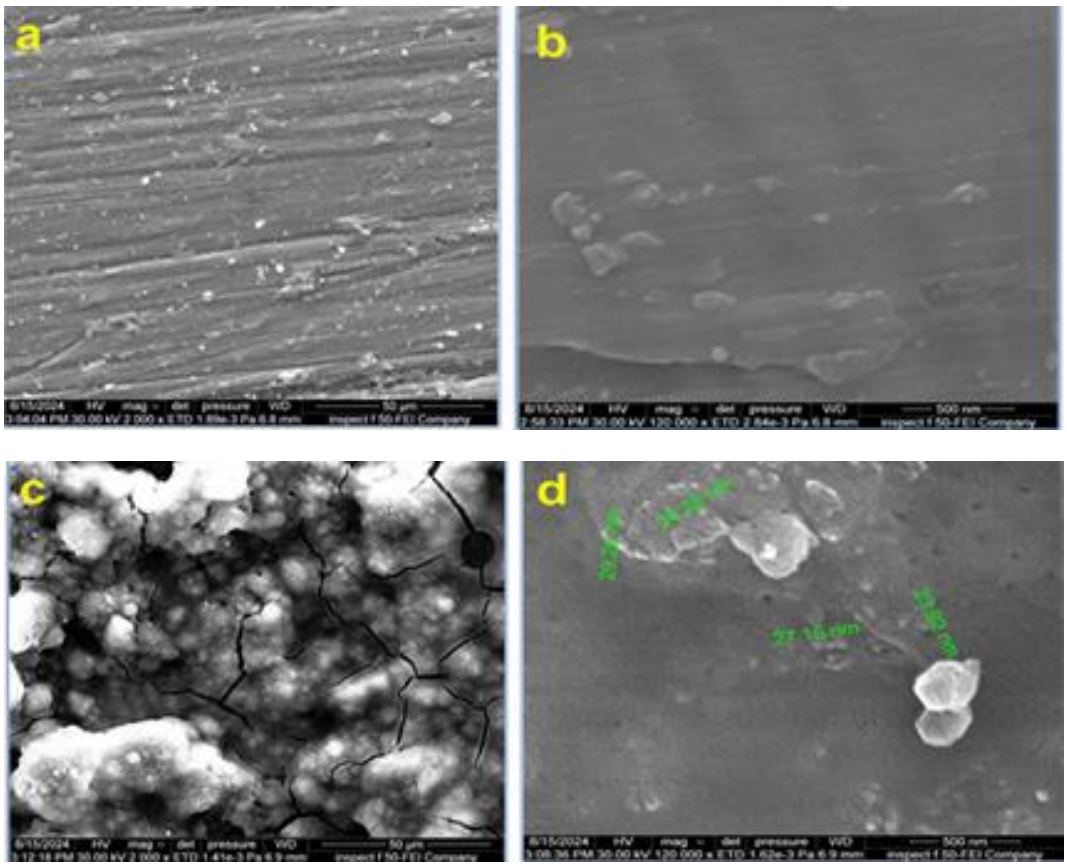

Figure 9: FESEM images for all samples (a, b): uncoated, (c, d): 2 layers, (e, f): 3 layers, (g, h): 4 layers, and (I, j): 5 layers.

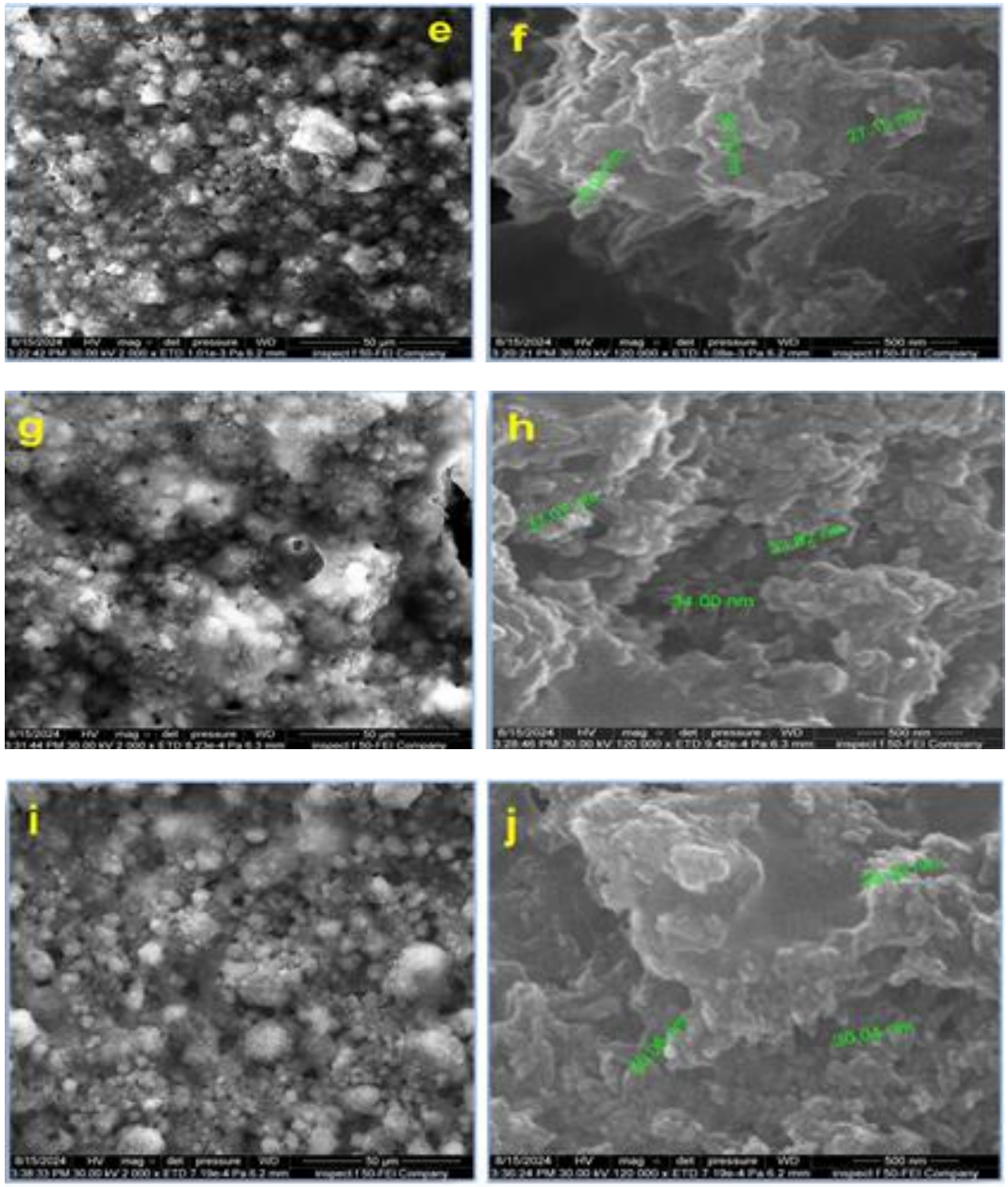

Figure 9: Continue.

3.3. EDX test

The EDX test for the 5-layer coated and uncoated samples in Figures 10a and b shows the presence of titanium, niobium, and zirconium as the main components for the uncoated sample. However, for the 5-layer coated sample, the main components were calcium, phosphorus, and oxygen, with no appearance of titanium, niobium, or zirconium. This occurred because the coating uniformly covered the surface and obstructed the appearance of the alloy elements.

3.4. Corrosion test

Electrochemical techniques to evaluate corrosion resistance are widely employed to predict the protective characteristics of certain biocompatible alloys [35]. The OCP test for all samples in Figure 11 and Table 4 shows an increase in OCP values, indicating that the coating makes the samples more passive. The OCP curves for all samples exhibited a slight increase over 1200 seconds. Analysis of the electrochemical parameters revealed that as the HAp layers increased, the Eocp shifted to more positive values, ranging from -0.610 to -0.300 V.

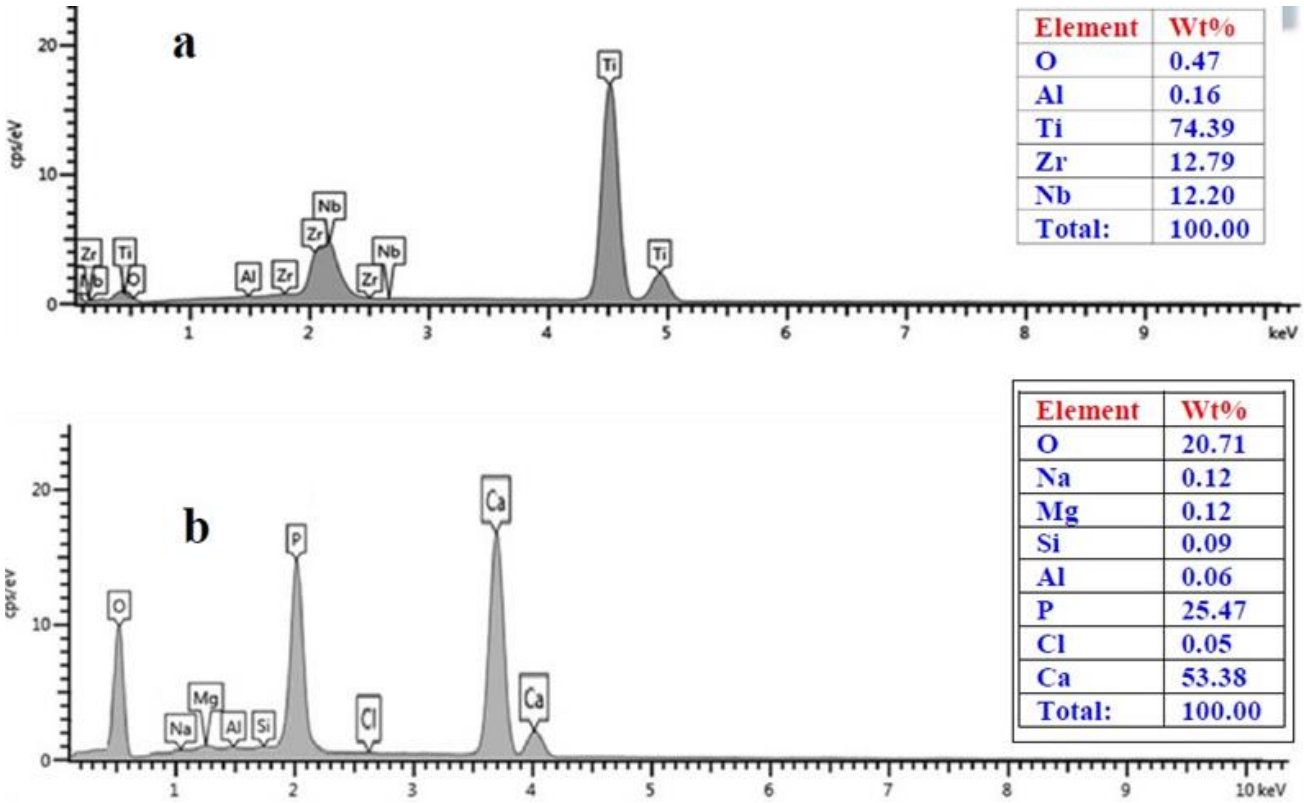

Figure 10: EDX test for a: uncoated $Ti_{13}Nb_{13}Zr$ alloy, b: 5-layer coated sample.

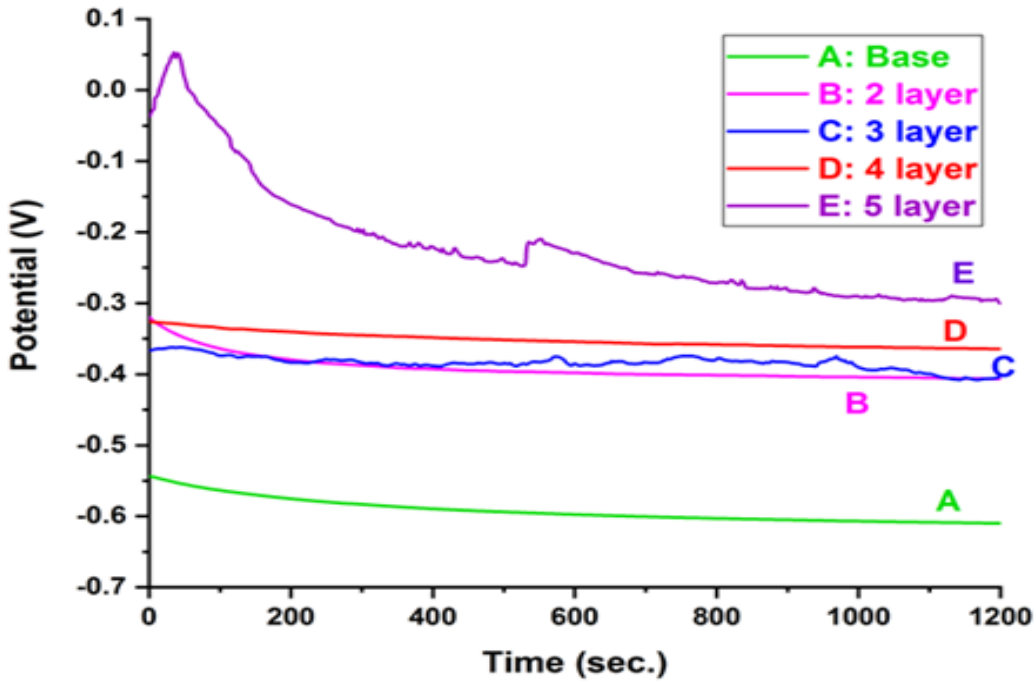

Figure 11: OCP testing for all samples.

Table 4: OCP test results for all samples.

ITEM	OCP (Volt)
Base	-0.610
2layer HA	-0.407
3layer HA	-0.403
4layer HA	-0.364
5layer HA	-0.300

The polarization curve test for all samples discloses the improvement in corrosion characteristics with increasing number of coated layers, as shown in Figure 12 and Table 5. The corrosion rate was reduced from 1.741×10^{-3} mmpy for the uncoated sample to 5.779×10^{-5} mmpy for the 5-layer coated sample, i.e., a reduction in corrosion rate of about 30 times, and achieved protection efficiency of about 96 %.

The protection efficiency can be calculated from the following equation (Eq. 1) [36]:

$$PE\ \% = \frac{icorr.uncoated - icorr.\ coated}{icorr.\ uncoted} \times 100 \quad (1)$$

Where PE % denotes protection efficiency, i_{corr}, uncoated refers to the corrosion current for the uncoated sample, and i corr. coated indicates the corrosion current for the coated sample. The Resistance of Polarization (Rp) can be determined according to the Stern-Geary equation below (Eq. 2) [37]:

$$Rp = \frac{ba \times bc}{2.303(ba+bc)icor.} \quad (2)$$

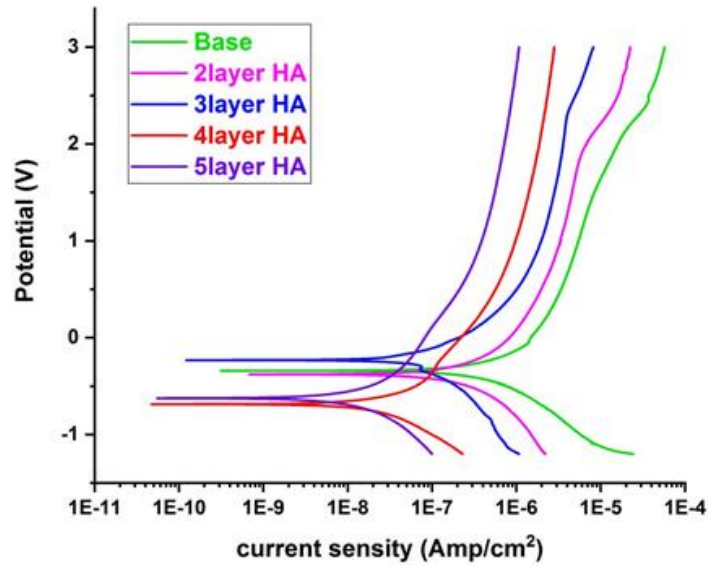

Figure 12: Polarization curve (Tafel) for all samples.

Table 5: Corrosion characteristics for all samples.

ITEM	E corr. (volt)	I corr. (Amp.)	Corr. Rate (mpy)
Base	-0.331	1.971×10^{-7}	1.741×10^{-3}
2layer HA	-0.386	9.390×10^{-8}	8.296×10^{-4}
3layer HA	-0.224	4.532×10^{-8}	4.004×10^{-4}
4layer HA	-0.675	1.324×10^{-8}	1.169×10^{-4}
5layer HA	-0.628	6.541×10^{-9}	5.779×10^{-5}

Where Rp is the resistance of polarization (Ω/cm²), ba is the Tafel slope for the anodic region, bc is the Tafel slope for the cathodic region, and i_{corr} is the corrosion current density (A/cm²). The calculated protection efficiency for uncoated and coated samples in Table 5 shows an increase in protection efficiency from 52.35 % for the 2-layer coated sample to 96.68 % for the 5-layer coated sample. That is, the protection efficiency increased gradually with an increasing number of coating layers. Additionally, hydroxyapatite improved the corrosion resistance of the coated samples. The calculated resistance of polarization for uncoated and coated samples in Table 6 shows a gradual increase in resistance of polarization from 2.21354×10^5 (Ω/cm²) for the uncoated sample to 6.654600×10^6 (Ω/cm²) for the 5-layer coated sample. This occurs because the increasing number of coated layers intuitively obstructs the corrosion media from reaching the alloy surface, increasing the polarization resistance.

The electrochemical impedance test (EIS) for uncoated and five-layer samples in Figure 13a shows a semicircular curve for both samples, along with a typical fitted Randles equivalent circuit for the uncoated sample in Figure 13b. Meanwhile, the five-layer coated sample exhibits a different model for the fitted equivalent circuit, as shown in Figure 13c.

The equivalent circuit for the uncoated sample shows solution resistance (R_s), which was simulated by body fluid (SBF) in our test, the electric double layer constant phase element (CPEdl), and the charge transfer resistance (R_{ct}). In contrast, the equivalent circuit for the 5-layer coated sample includes the previous elements along with the coating constant phase element (CPEc) and the coating resistance (Rc). The second model refers to a porous coating layer. From Table 6, which presents the EIS test fitted model results, we observe that the total resistance increased from 2373.23 ohms for the uncoated sample to 18492.4 ohms for the 5-layer coated sample, which is approximately 7 times higher.

Table 6: Calculated protection efficiency and resistance of polarization for coated samples.

ITEM	i corr.(Amp.)	PE %	βC	βa	Rp(Ω/cm²)
Base	1.971×10^{-7}	--------	0.198	0.204	2.21354×10^5
2layer HA	9.390×10^{-8}	52.35	0.209	0.203	4.76196×10^5
3layer HA	4.532×10^{-8}	77.00	0.120	0.185	6.97379×10^5
4layer HA	1.324×10^{-8}	93.28	0.223	0.188	3.354533×10^6
5layer HA	6.541×10^{-9}	96.68	0.202	0.199	6.654600×10^6

Table 7: EIS test fitted models results.

Parameters	Uncoated sample	5 layers coated sample
Rs (Ω/cm²)	355.63	286.9
Rdl (Ω/cm²)	2017.6	304.5
Rc (Ω/cm²)	-	17901
CPEdl (μF cm^{-2})	1.3266×10^{-5}	8.9236×10^{-6}
n1	0.96412	0.94221
CPEc (μF cm^{-2})	-	3.6751×10^{-5}
n2	-	0.9805
Rtotal (Ω/cm²)	2373.23	18492.4

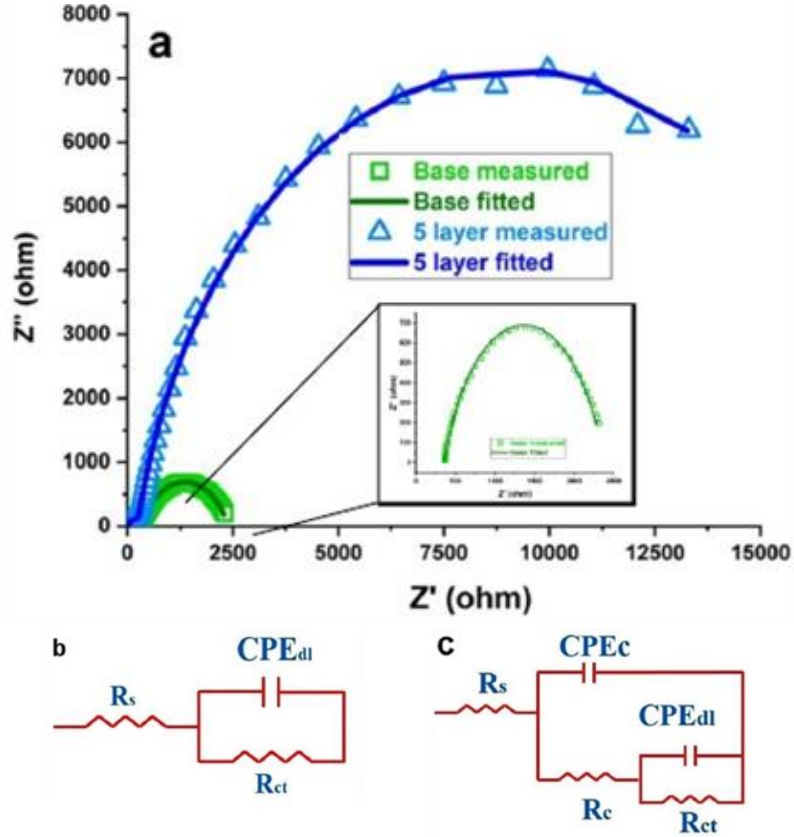

Figure 13: EIS test for uncoated and 5-layer samples with equivalent fitted circuit, a) Nyquist diagram comparison, b) fitted equivalent circuit model for uncoated sample, and c) fitted equivalent circuit model for 5-layer sample.

Figure 14: Photo of the original device value.

3.5. Adhesion test

In this research, the standard adhesion cross-cut tape test, ASTM D3359, was adopted to evaluate the adhesion of coated samples. Figure 15 and Table 8 show the increase in adhesion with an increasing number of coated layers. The 5-layer sample achieved the highest adhesion characteristic, with a minimum removed area reaching 0% and a classification of 5B, while the other samples showed an increase in removed area with a decreasing number of coated layers.

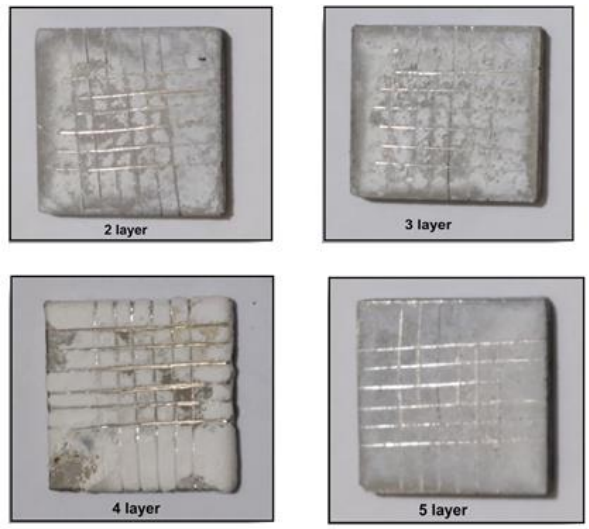

Figure 15: The adhesion test images for all coated samples.

Table 8: The adhesion test results according to ASTM D3359.

Item	Classifictin	Percentage area removed
1- 2layer HA	2B	28%
2- 3layer HA	2B	16%
3- 4layer HA	3B	10%
4- 5layer HA	5B	0%

3.6. Wettability contact angle test

Some in vitro methods, such as the contact angle test, can be used to assess biocompatibility [38]. The formation of hydrophilicity is critical for cell adhesion, proliferation, and differentiation on the surface of the material [39]. It is known that hydrophilic surfaces with a water contact angle of less than 60° support cell attachment [40]. Previous studies have reported that the contact angle value of Ti is usually above 60°. The contact angle was reduced by adding HA to Ti or by coating the surface of Ti with HA [41]. The wettability contact angle test in Figure 16 and Table 9 shows very close values for the coated samples, with a slight increase in contact angle as the number of coating layers increases. This occurred because the increase in the number of coating layers decreases porosity and cracks, as observed previously in the FESEM test. Additionally, the increase in the number of coating layers raises the PVP quantity, which enhances hydrophobic properties. Therefore, all these reasons contributed to the slight increase in the wettability contact angle.

3.7. After immersing in the SBF solution

3.7.1. XRD test

Figure 17 represents the XRD pattern for the uncoated sample after immersion in SBF solution for one month and shows the peaks of hydroxyapatite and titanium. The peaks of hydroxyapatite perfectly match JCPDS File Card No. 00-009-0432 for hydroxyapatite, while the three peaks of the $Ti_{13}Nb_{13}Zr$ alloy match JCPDS File Card No. 00-044-1294 for titanium.

Table 9: Wettability contact angle for all samples.

ITEM	Wettability contact angel degree
1- Base	76.620
2- HA 2layer	12.862
3- HA 3layer	15.336
4- HA 4layer	17.312
5- HA 5layer	18.100

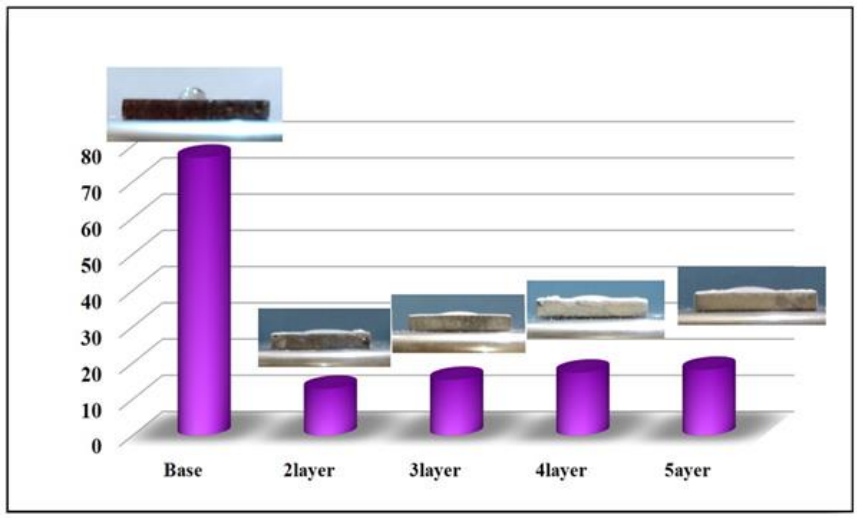

Figure 16: Wettability contact angle for all samples.

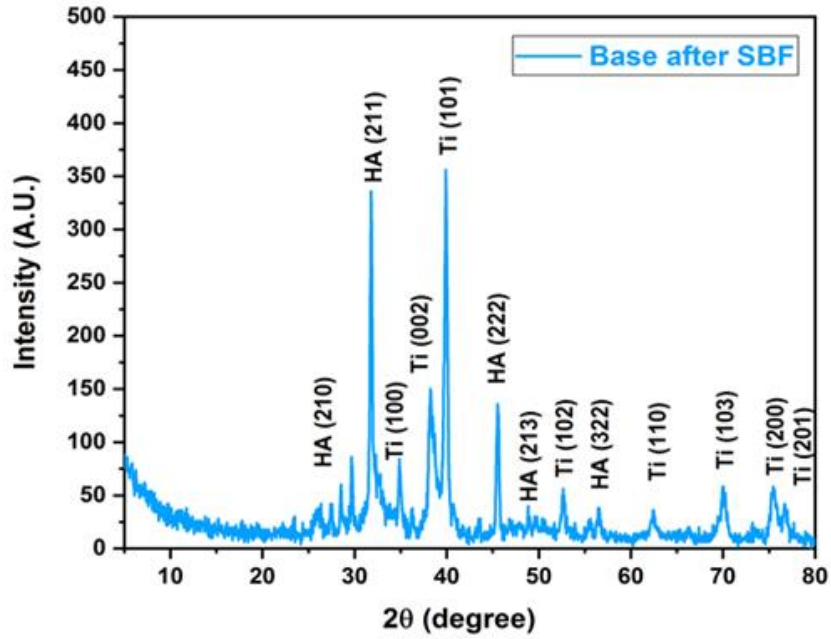

Figure 17: XRD pattern for the uncoated sample after immersing in SBF solution for one month.

The appearance of hydroxyapatite peaks on the surface of the $Ti_{13}Nb_{13}Zr$ base is an indicator of bone osseointegration. The XRD pattern for the five-layer sample after immersing it in SBF solution for one month, shown in Figure 18, indicates the appearance of hydroxyapatite that matches JCPDS File Card No. 00-009-0432. This occurred because the new hydroxyapatite layer formed from the SBF solution after one month covered the surface very well, serving as a good indicator for bone osseointegration as well.

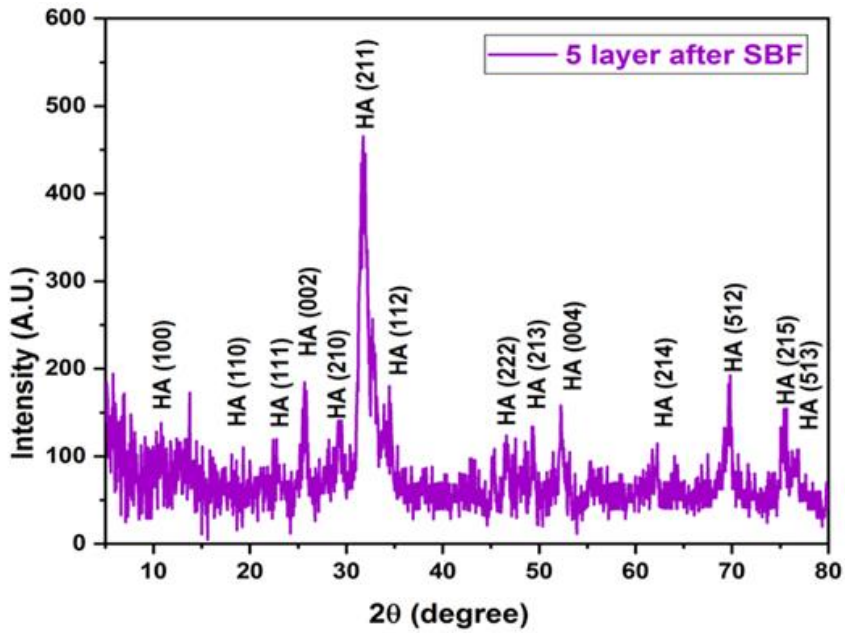

Figure 18: XRD pattern for 5-layer sample after immersing in SBF solution for one month.

3.7.2. FFESEM test

The FESEM images for uncoated base and five-layer samples after immersion in SBF solution for one month, shown in Figure 19a-d, exhibit a very different morphology compared to before immersion. The base sample clearly shows the appearance of a thick new hydroxyapatite layer formed from the SBF solution, which has many cracks. These cracks explain the appearance of titanium peaks in the previous XRD test. The cracks occurred because the metal base expands faster than the ceramic layer during the sintering process. The particle size measured from FESEM images for the new hydroxyapatite layer varied between 82.6 nm and 48.57 nm. The five-layer sample shows the formation of a very uniform hydroxyapatite layer without any cracks covering the entire surface, which explains the dis-appearance of titanium peaks in the previous XRD test. The particle size varied between 62.2 nm and 46.2 nm.

3.7.3. EDX test

The EDX test for the uncoated sample, after immersion in SBF solution for one month, as shown in Figure 20a, reveals the presence of calcium, phosphorus, and oxygen, indicating the formation of hydroxyapatite. Additionally, silicon, chlorine, potassium, magnesium, sodium, and sulfur appear as trace elements in the hydroxyapatite formed from the SBF solution. The presence of titanium, zirconium, and niobium originates from the base alloy, which is evident due to the cracks in the hydroxyapatite layer. The five-layer coated sample in Figure 20b also shows mostly the same elements as the uncoated sample, but without the presence of titanium, zirconium, and niobium, as the coating layer effectively covers the surface.

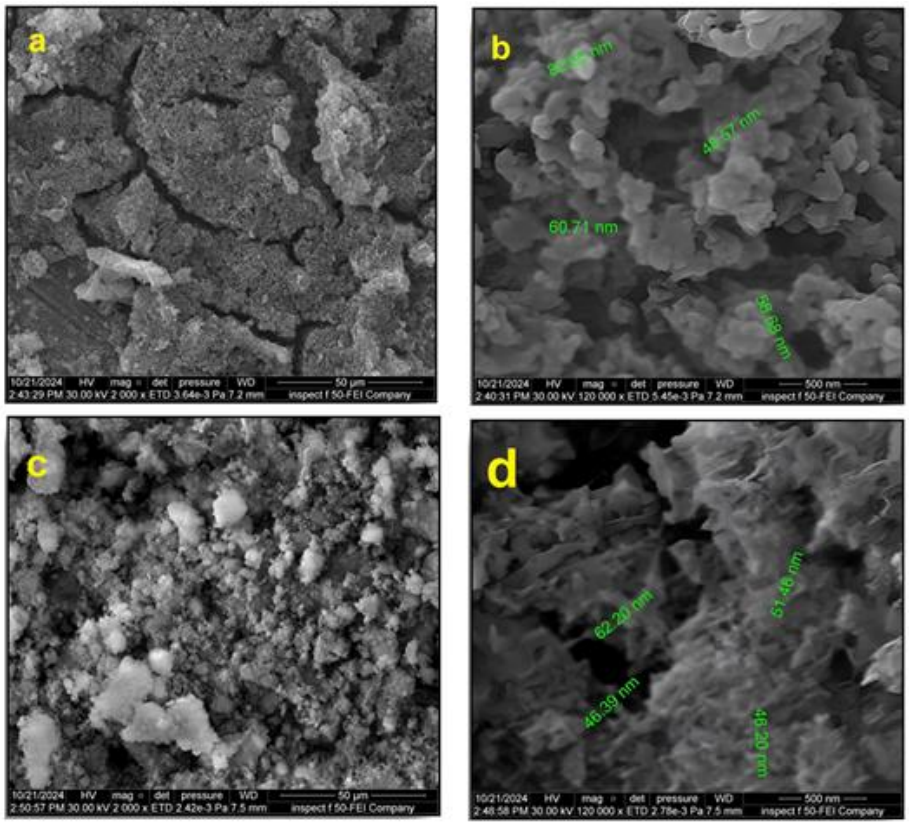

Figure 19: FESEM Images of the foruncoated base and 5-layer samples after immersing in SBF solution for one month.

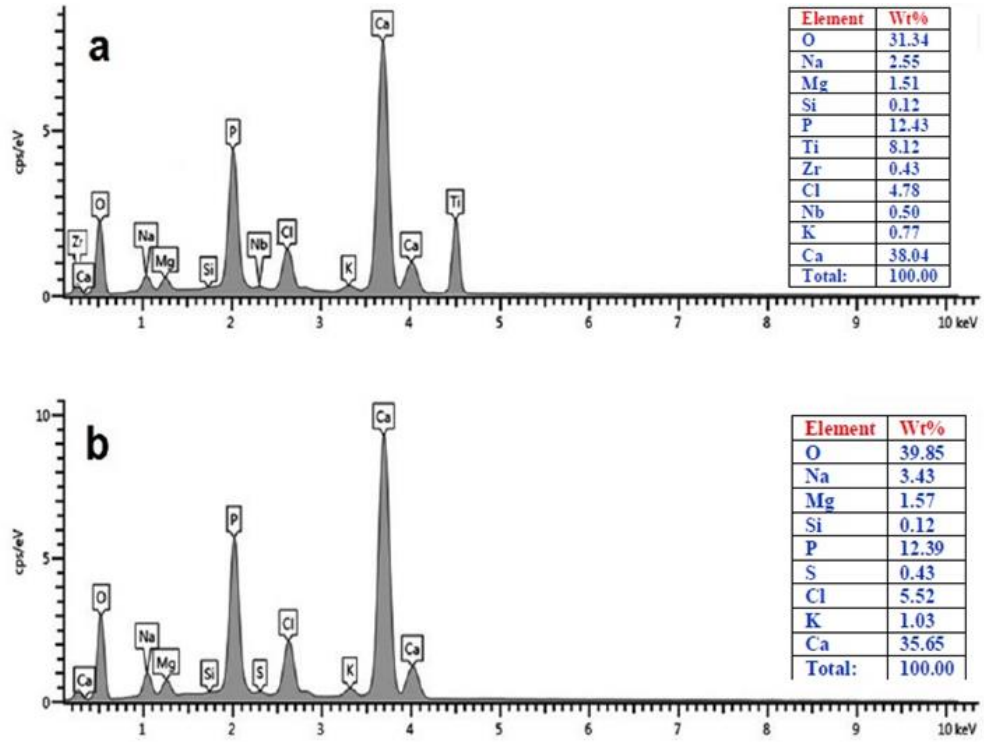

Figure 20: EDX test after immersing in SBF solution for one month for a: uncoated sample, 5-layer coated sample.

3.7.4. Corrosion test

Figure 21, which represents the OCP test for uncoated and five-layer coated samples after immersion in SBF solution, shows an increase in OCP values for both samples compared to the values before immersion. The OCP for the uncoated sample after immersion is -0.442 volts, compared to -0.610 volts before immersion, and the OCP for the five-layer coated sample is -0.231 volts, compared to -0.300 volts before immersion. This indicates that passivation increased after immersion in the SBF solution. The polarization curve Tafel test for uncoated and five-layer coated samples, after immersion in SBF solution, shows a decrease in the corrosion rate for both samples, as shown in Figure 22 and Table 10. The corrosion rate for the uncoated sample decreased from 1.741×10^{-3} mmpy to 6.891×10^{-4} mmpy, while the corrosion rate for the five-layer coated sample decreased from 5.779×10^{-5} mmpy to 3.498×10^{-5} mmpy.

The calculation of protection efficiency for uncoated and five-layer coated samples after immersion in SBF solution shows an increase in efficiency when a new hydroxyapatite layer forms from the SBF solution and covers the surface of the sample, as shown in Table 11. The protection efficiency for the uncoated sample increased to 60.04 % after immersion in the SBF solution, compared with 0 % for the uncoated sample before immersion. The protection efficiency of the five-layer coated sample increased from 96.68 % before immersion to 98.27 % after immersion. The resistance of polarization for the uncoated sample increased from 2.21354×10^5 (Ω/cm^2) before immersion to 5.266208×10^5 (Ω/cm^2) after immersion in SBF solution. Additionally, the resistance of polarization for the five-layer coated sample increased from 6.654600×10^6 (Ω/cm^2) to 1.3232386×10^7 (Ω/cm^2) after immersion in SBF solution. This indicates that the new coated layer serves as a new hurdle for the corrosive solution to reach the alloy surface.

Table 10: Corrosion characteristics for uncoated and 5-layer coated samples after immersing in SBF solution.

ITEM	E corr. (volt)	I corr. (Amp.)	Corr. Rate Mmpy
Base	-0.407	7.803×10^{-8}	6.891×10^{-4}
5layer HA	-0.197	3.396×10^{-9}	3.498×10^{-5}

Table 11: Calculated protection efficiency and resistance of polarization for coated samples.

ITEM	i_{corr} (Amp.)	PE %	βC	βa	Rp (Ω/cm^2)
Base	7.803×10^{-8}	60.04	0.204	0.203	5.266208×10^5
5layer HA	3.396×10^{-9}	98.27	0.205	0.209	13232386×10^7

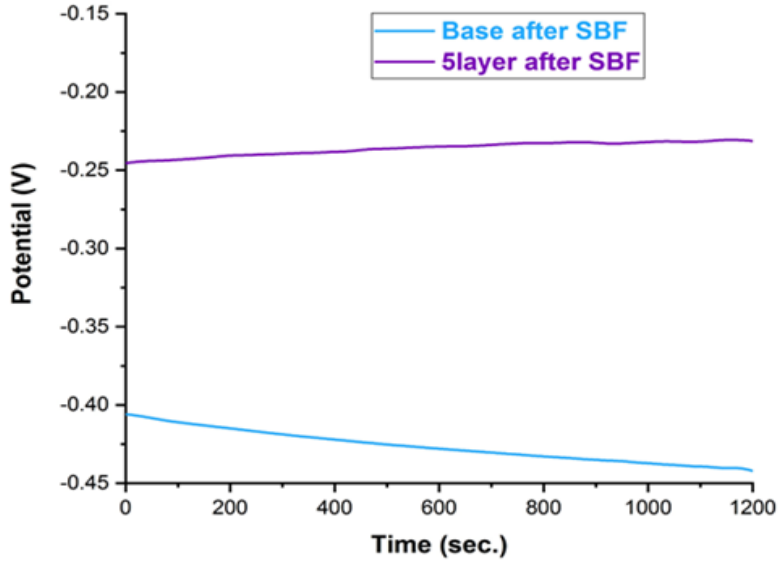

Figure 21: OCP curve for uncoated and 5-layer coated samples after immersing in SBF solution.

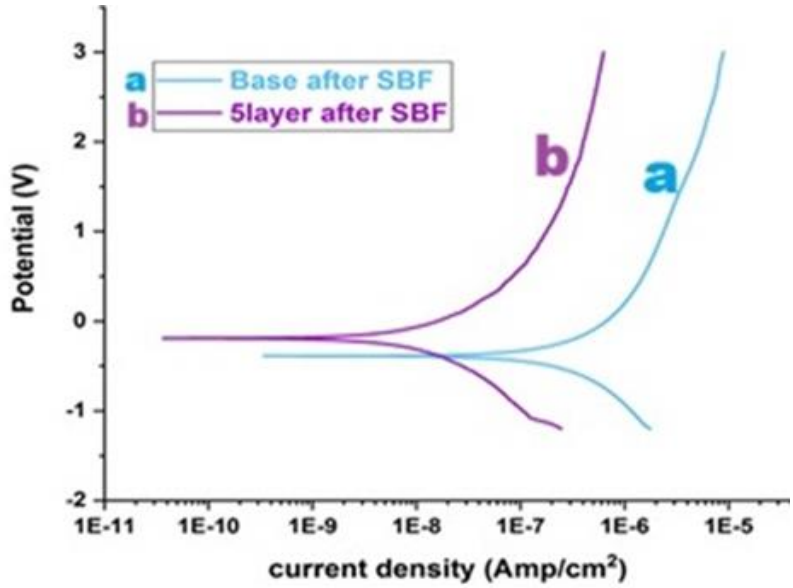

Figure 22: Tafel curve for uncoated and 5-layer coated samples after immersing in SBF solution.

The EIS test for uncoated and five-layer coated samples after immersion in SBF solution shows a distinct new equivalent circuit for the uncoated sample, resulting from the new hydroxyapatite formed from the SBF solution, as shown in Figures 23a and b. This refers to the formation of a new porous layer, where the Nyquist curve displays a first semicircle for the new layer formed and part of a second semicircle for

the double layer impedance. Additionally, the total resistance increased from 2,373.23 ohms before immersion to 10,572.62 ohms after immersion for the uncoated sample, as shown in Table 12. The EIS test for the five-layer coated samples after immersion in SBF shows a first semicircle for the new hydroxy-apatite formed from the SBF solution and part of a second semicircle for the previously coated layer and double layer impedance. We also observe a change in the equivalent circuit, indicating that a new porous layer was added, as shown in Figure 20c. The total resistance increased from 18,492.4 ohms to 35,860.3 ohms, as shown in Table 12.

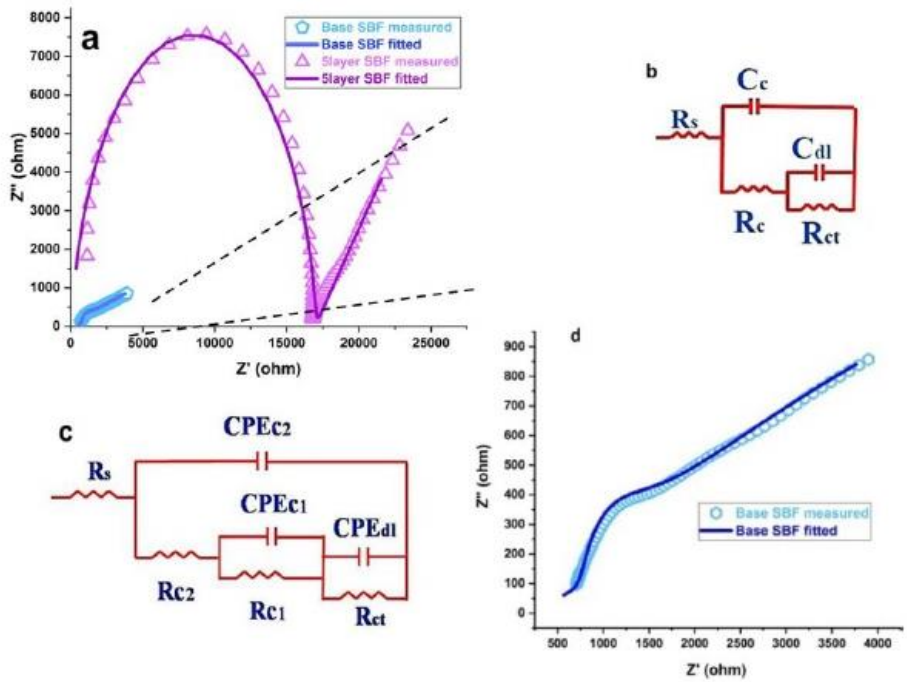

Figure 23: EIS test for uncoated and 5- layer samples after immersing in SBF solution with equivalent fitted circuit a: Nyquist diagram comparison, b: fitted equivalent circuit model for uncoated sample, c: fitted equivalent circuit model for 5- layer sample and d: EIS test for uncoated after immersing in SBF solution.

Table 12: EIS test fitted models results for uncoated and 5-layer coated samples after immersing in SBF solution.

Parameters	Uncoated sample	5 layers coated sample
Rs (Ω/cm^2)	322.02	155.3
Rdl (Ω/cm^2)	1986	1019
Rc1 (Ω/cm^2)	8264.6	1.7819×10^{4}
Rc2 (Ω/cm^2)	--------	1.6867×10^{4}
CPEdl ($\mu F\ cm^{-2}$)	5.4912×10^{-4}	2.7134×10^{-8}
n1	0.96298	0.988674
CPEc1 ($\mu F\ cm^{-2}$)	3.1704×10^{-7}	5.1095×10^{-6}
n2	0.99069	0.95093
CPEc2 ($\mu F\ cm^{-2}$)	------	8.4387×10^{-6}
n3	------	0.92772
R_{total} (Ω/cm^2)	10572.62	35860.3

4. Conclusion

From previous results, we conclude that the corrosion rate improved and reached 3.498×10^{-5} mmpy for the five-layer sample after immersion in SBF solution for a month, compared to 1.741×10^{-3} mmpy for the uncoated sample before immersion in SBF solution. This indicates that the corrosion rate decreased by about 50 times. The protection efficiency reached 98.27 %, and the polarization resistance reached 1.3232386×10^{7} (Ω/cm^2) compared to 2.21354×10^{5} (Ω/cm^2) for the five-layer sample after immersion in SBF solution for a month. The total resistance for the five-layer sample after immersion in SBF solution for a month reached 35860.3 ohms, compared to 2373.23 ohms for the uncoated sample before immersion. Additionally, the XRD test shows the appearance of HAP peaks with high intensity, and all peaks of titanium disappeared, indicating the formation of a new hydroxyapatite layer from the SBF solution. The FESEM images show this new layer, which means we achieved a good osseointegration indicator. The corrosion studies using potentiodynamic polarization measurements as well as EIS techniques show that HAP coatings exhibit significantly improved corrosion resistance properties compared to those of the uncoated sample. This investigation is particularly noteworthy since we used a cost-effective, straight-forward spray pyrolysis technique to obtain HAP.

5. References

1. Khorasani A M, Goldberg M, Doeven, Egan H, Littlefair G. Titanium in biomedical applications-properties and fabrication: a review. J Biomater Tissue Eng. 2015; 5:593-619. https://doi:10.1166/jbt.2015. 1361.
2. Yassin MA, Khairul Salleh M S, Mahadzir I, Basim A K. Titanium and its alloy. Inter J Sci Res (IJSR). 2014; 3(10):1351-1361.
3. EliaMarin AL. Biomedical applications of titanium alloys: A comprehensive review. Materials. 2024; 17(1): 114. https://doi.org/10.3390/ma17010114.
4. Veiga C, Davim JP, Loureiro AJR. Properties and applications of titanium alloys: A brief review. Rev Adv Mater Sci. 2012; 32: 133-148.
5. Alicja K, Izabela K, Wojciech S. Anodization of a medical-grade Ti-6Al-7Nb alloy in a $Ca(H_2PO_2)_2$-hydroxyapatite suspension. Materials. 2019; 12(18): 3002. https://doi.org/10.3390/ma12183002
6. Büyüksağiş A, Bulut E, Kayalı Y. Corrosion behaviors of hydroxyapatite coated by electrode-position method of Ti_6Al_4V, Ti and AISI 316L SS substrates. Physicochem Problem Mater Protect. 2013, 49(6):775-786. https://doi.org/10.1134/S207020511 306018X.
7. Jażdżewska M, Majkowska BM. Hydroxyapatite deposition on the lasermodified $Ti1_3Nb1_3Zr$ alloy. Adv Mater Sci. 2017; 17(4):5-13. https://doi.org/10. 1515/adms-2017-0017.
8. Safaa N, Adilla EM, Randa RA. Structural and morphological features of hydroxyapatite nano-particles from different calcium resources. Aswan University J Environ Stud (AUJES). 2022;3(3):313-323.https://doi.org/10.21608/aujes.2022.142530.1070.
9. Hui S, Ziqi Z, Wuda L, Yuan F, Zhihua L, Junchao W. Hydroxyapatite based materials for bone tissue engineering: A brief and comprehensive introduction. Crystals. 2021;11(2):149. https://doi.org/10.3390/cryst 11020149.
10. Vivekanand SK, Sudheer K, Krishna PL. Hydroxyapatite—past, present, and future in bone regeneration. Bone Tissue Regen Insights. 2016; 7: 9-19. https://doi.org/10.4137/BTRI.S36138.
11. RebazObaid K, Niyazi B, Omer K. Hydroxyapatite biomaterials: A comprehensive review of their properties, structures, medical applications, and fabrication methods. J Chem Rev. 2024; 6(1):1-26. https://doi. org/10.48309/jcr.2024.415051.1253.
12. Mohan L, Durgalakshmi D, Geetha M, Sankara Narayanan TSN, Asokamani R. Electrophoretic deposition of nanocomposite ($HAp+TiO_2$) on titanium alloy for biomedical applications. Ceram Inter. 2012; 38(4):3435-3443. https://doi.org/10.1016/j.ceramint. 2011. 12.056.
13. Deram V, Minichiello C, Vannier RN, Maguer A, Pawlowski L, Murano D. Microstructural characterizations of plasma sprayed hydroxyapatite coatings. Surf Coat Technol. 2003;166(2-3):153-159. https://doi. org/10.1016/S0257-8972(02)00855-1.
14. Kubie LS, Shults GM. Studies on the relationship of the chemical constituents of blood and cerebrospinal fluid. J Exp Med. 1925; 42(4):565-591. https://doi. org/10.1084/jem.42.4.565.
15. Sandra CPC, Rui NC. Titanium scaffolds for osteointegration: Mechanical, in vitro and corrosion behavior. J Mater Sci Mater Med. 2008; 19: 451-457. https://doi.org/10.1007/s10856-006-0052-7.
16. Akram M, Ahmed R, Shakir I, Ibrahim WAW, Hussain R. Extracting hydroxyapatite and its precursors from natural resources. J Mater Sci. 2014;49:1461-1475. https://doi.org/10.1007/s10853-013- 7864-x.
17. Milovac D, Gamboa-martínez TC, Ivankovic M, Gallego G, Ivankovic H. PCL coated hydroxyapatite scaffold derived from cuttle fish bone: In vitro cell

culture studies. Mater Sci Eng C. 2014; 42:264-272. https://doi.org/10.1016/j.msec.2014.05.034.
18. Ahmadi R, Asadpourchallou N, Kaleji BK. In vitro study: Evaluation of mechanical behavior, corrosion resistance, antibacterial properties and biocompatibility of HAp/TiO_2/Ag coating on Ti_6Al_4V/TiO_2 substrate. Surf Interfaces. 2021;24:101072. https://doi.org/10.1016/j.surfin.2021.101072.
19. Wang Z, Ye F, Chen L, Lv W, Zhang Z, Zang Q, Lu S. Preparation and degradation characteristics of MAO/APS composite bio-coating in simulated body fluid. Coatings. 2021;11(6):667. https://doi.org/10.3390/coatings11060667.
20. Heimann RB. Structural changes of hydroxylapatite during plasma spraying: raman and NMR spectroscopy results. Coatings. 2021;11(8):987. https://doi.org/10.3390/coatings11080987.
21. Farooq SA, Raina A, Mohan S, Arvind SR, Jayalakshmi S, Irfan UlHaq M. Nanostructured coatings: Review on processing techniques, corrosion behaviour and tribological performance. Nanomaterials. 2022; 12(8):1323. https://doi.org/10.3390/nano12081323.
22. Bora Mavis A, Cuneyt T. Dip coating of calcium hydroxyapatite on Ti-6Al-4V Substrates. J Am Ceram Soc. 2000;83(4):989-991. https://doi.org/10.1111/j.1151-2916.2000.tb01314.x
23. Balbina M, Agnieszka O. Electrophoretically deposited titanium and its alloys in biomedical engineering: Recent progress and remaining challenges. J Biomed Mater Res. 2023;112(1): e35342. https://doi.org/10.1002/jbm.b.35342.
24. Sheng D, Mengchao C, Jiahui L, Meng Zh. Cold spray technology and its application in the manufacturing of metal matrix composite materials with carbon-based reinforcements. Coatings. 2024; 14(7): 822. https://doi.org/10.3390/coatings14070822.
25. Gaurav P, Hitesh V. Thermal sprayed composite coatings for biomedical implants: A brief review. J Thermal Spray Eng. 2020; 2(1):50-55. https://doi.org/10.52687/2582-1474/213.
26. Kozhukharov S, Tchaoushev S. Spray pyrolysis equipment for various applications. J Chem Technol Metal. 2013; 48(1):111-118.
27. Christos D, Pavlos P, Maria S, Yiannis D. Advanced flame spray pyrolysis (FSP) technologies for engineering multifunctional nanostructures and nanodevices. Nanomaterials. 2023;13(23):3006. https://doi.org/10.3390/nano13233006.
28. Charmelle DS, Ernst EF, Julian S, Holger L. A review of using spray pyrolysis through sol-gel materials in the synthesis of cathode materials for lithium-ion batteries. S Afr J Chem. 2016; 69:88-97.
29. Ashish A, Siddhartha D, Shreya V, Mahesh KS. Advancement in harnessing fish waste for cutting-edge hydroxyapatite in bone regeneration. Emergent Mater. 2024; 7:2305-2322. https://doi.org/10.1007/s42247- 024-00782-2.
30. Zheng Z, Wu S, Shu H, Han Q, Cao P. Layer-by-layer self-assembly marine antifouling coating of phenol absorbed by polyvinylpyrrolidone anchored on stainless steel surfaces. J Mar Sci Eng. 2025; 13(3): 568. https://doi.org/10.3390/jmse13030568.
31. Beata B, Maciej T, Tomasz C. Polyvinylpyrrolidone-based coatings for polyurethanes-the effect of reagent concentration on their chosen physical properties. Chem Proc Eng. 2012;33(4):563-571. https://doi.org/10. 2478/v10176-012-0046-6.
32. Kokubo T, Takadama H. How useful is SBF in predicting in vivo bone bioactivity?. Biomaterials. 2006; 27(15):2907-2915. https://doi.org/10.1016/j.biomaterials.2006.01.017.
33. Xuanyong L, Chuanxian D, Paul KChu. Mechanism of apatite formation on wollastonite coatings in simulated body fluids. Biomaterials. 2004;25(10): 1755-1761. https://doi.org/10.1016/j.biomaterials. 2003. 08.024.
34. Anene FA, Jaafar CNA, Mohamed Ariff AH, Zainol I, Mohd Tahir S, Abdul Razak B, Salit MS, Anene-Amaechi J. Biomechanical properties and corrosion resistance of plasma-sprayed fish scale hydroxyapatite (FsHA) and FsHA-doped yttria-stabilized zirconia coatings on Ti–6Al–4V alloy for biomedical applications. Coatings. 2023;13(1):199. https://doi.org/ 10.3390/coatings13010199.
35. Al-Mobarak NA, Al-Swayih AA, Al-Rashoud FA. Corrosion behavior of Ti-6Al-7Nb alloy in biological solu-tion for dentistry applications. Inter J Electrochem Sci. 2011;6(6):2031-2042. https://doi.org/10.1016/ S1452-3981(23)18165-X
36. Khulood AbidSaleh A, Al-Mashhdani HAY. Corrosion protection study for caron steel in seawater by coating with SiC and ZrO_2 Nanoparticles. Am J Chem. 2015;5(1):28-39. https://doi.org/10.5923/j.chemistry. 20150501.05
37. Bobic B, Mitrovic S, Babic M, Vencl A, Bobic I. Corrosion behavior of the As-cast and heat-treated ZA27 Alloy. Tribol Indust. 2011; 33(2): 87-93.
38. Gao YL, Liu Y, Song XY. Plasma-sprayed hydroxyapatite coating for improved corrosion resistance and bioactivity of magnesium alloy. J Therm Spray Technol. 2018; 27(8): 1381-1387. https://doi.org/10.1007/s11666-018-0760-9.
39. Anjaneyulu U, Priyadarshini B, Arul Xavier Stango S, Chellappa M, Geetha M, Vijayalakshmi U, Preparation and characterization of sol–gel-derived hydroxyapatite nanoparticles and its coatings on medical grade Ti-6Al-4V alloy for biomedical applications. Mater. Technol. 2017, 32(13):800-814. https://doi.org/10.1080/10667857.2017.1364476.
40. Cotrut M, Vladescu A, Dinu M, Vranceanu DM. Influence of deposition temperature on the properties of hydroxyapatite obtained by electrochemical assisted deposition. Ceram Int. 2018;44(1):669-677.https://doi.org/10.1016/j.ceramint.2017.09.227.
41. Odusote K, Danyuo Y, Baruwa AD, Azeez AA. Synthesis and characterization of hydroxyapatite from

bovine bone for production of dental implants. J Appl Biomater Funct Mater. 2019; 17(2):222. https://doi.org/10.1177/2280800019836829.

42. Biguetti CC, Cavalla F, Silveira EM, Fonseca AC, Vieira AE, Tabanez AP, Rodrigues DC, Trombone APF, Garlet GP. Oral implant osseointegration model in C57Bl/6 mice: Microtomographic, histological, histomorphometric and molecular characterization. J Appl Oral Sci. 2017; 26: e20170601. https://doi.org/10.1590/1678-7757-2017-0601.

How to cite this article:
Hamed Farhan G, Abduljabar Hassan J, Al-helli AH. Coating $Ti_{13}Nb_{13}Zr$ alloy with hydroxyapatite using pyrolysis spray improves corrosion and osseointegration characteristics for biomedical applications (In-vitro study). Prog Color Colorants Coat. 2026;19(2):113-133. https://doi.org/10.30509/pccc.2025.167501.1376.